

Generative Adversarial Networks And Domain Adaptation For Training Data Independent Image Registration

Dwarikanath Mahapatra

*Inception Institute of Artificial Intelligence, Abu Dhabi, UAE
dwarikanath.mahapatra@inceptioniai.org*

Abstract

Medical image registration is an important task in automated analysis of multi-modal images and temporal data involving multiple patient visits. Conventional approaches, although useful for different image types, are time consuming. Of late, deep learning (DL) based image registration methods have been proposed that outperform traditional methods in terms of accuracy and time. However, DL based methods are heavily dependent on training data and do not generalize well when presented with images of different scanners or anatomies. We present a DL based approach that can perform medical image registration of one image type despite being trained with images of a different type. This is achieved by unsupervised domain adaptation in the registration process and allows for easier application to different datasets without extensive retraining. To achieve our objective we train a network that transforms the given input image pair to a latent feature space vector using autoencoders. The resultant encoded feature space is used to generate the registered images with the help of generative adversarial networks (GANs). This feature transformation ensures greater invariance to the input image type. Experiments on chest Xray, retinal and brain MR images show that our method, trained on one dataset gives better registration performance for other datasets, outperforming conventional methods that do not incorporate domain adaptation.

1. Introduction

Elastic (or deformable) image registration is crucial for many medical image analysis tasks such as computer aided diagnosis, atlas building, correcting deformations and monitoring pathological changes over time. It is especially relevant in monitoring patients over multiple visits and quantifying change of tumor volume and other pathologies. Such quantification gives an accurate estimate of treatment effectiveness. Deformable registration establishes a non-linear correspondence between a pair of images or 3-D image volumes. Conventional registration methods solve an optimization problem for each volume pair that aligns voxels with similar appearance while enforcing smoothness constraints on the registration mapping. This requires iterative gradient descent methods which are computationally intensive, and extremely slow in practice.

With the increasing number of works focusing on deep learning (DL) based image analysis, many interesting works on image registration have also been proposed. The method by [1, 2, 3, 4, 5, 6] learns a parameterized registration function from a collection of volumes, while there are other methods that use regression or generative models [7, 8, 9, 10, 11, 12, 13]. The primary shortcoming of current DL based image registration methods is a reliance on large *labeled* datasets for training. Although conventional registration methods are time consuming, they perform equally well on different types of image pairs. However, a DL network trained to register a pair of brain magnetic resonance (MR) images does not perform convincingly on a pair of chest xray images or vice-versa. Similar outcomes are observed if the test image is of the same anatomy but acquired using a different scanner. As a result, DL based image registration methods have to be retrained when presented with a new dataset. In general, it is challenging to obtain ground truth data for registration which restricts the method's use on new image types and in real world scenarios. In this paper we address the problem of using pre-trained registration networks on new datasets by proposing a domain adaptation based DL method that, once trained on a particular dataset, can be easily used on other image pairs with

minimal retraining.

The dataset independent registration is achieved by first using a network trained on a different dataset having ground truth correspondences for registration between source and target images. To enable transfer of knowledge across domains we use a latent feature space representation of the images and use them to generate the registered image instead of the original images. The latent feature representation is obtained from autoencoders and then fed to a generator network that generates the registered image and the deformation field. Previous work in [14, 15, 16, 17, 18, 19] demonstrates that between autoencoders and spiking neural networks, autoencoders do a better job for unsupervised visual feature learning. Hence we use them for obtaining a latent space representation with sufficiently discriminative features. The generated images are used as input to a discriminator that determines its accuracy and realism.

1.1. Related Work

We refer the reader to [20, 21, 22, 23, 24, 25] for a comprehensive review on conventional image registration methods. Although widely used, these methods are very time consuming, especially when registering image volumes. This is due to: 1) the iterative optimization techniques common to all methods; and 2) extensive parameter tuning involved. On the other hand, DL methods can potentially overcome these limitations by using trained models to output the registered images and the deformation field in much less time.

Since we propose a deep learning approach we review image registration methods that use it as part of their pipeline. Wu et. al. [26, 27, 28, 29, 30] used convolutional stacked autoencoders (CAE) to extract features from fixed and moving images, which are used in a conventional iterative deformable registration framework. Miao et. al. [31, 32, 33, 34, 35, 36] use convolutional neural network (CNN) regressors to rigidly register synthetic images. Liao et. al. [37, 38, 39, 40, 41, 42] use CNNs and reinforcement learning for iterative registration of CT to cone-beam CT in cardiac and abdominal images. FlowNet [43, 44, 45, 46, 47, 48] formulates dense optical flow estimation as a regression

task using CNNs and uses it for image matching. These approaches still use a conventional model to generate the transformed image from the deformation field which increases computation time and does not fully utilize the generative capabilities of DL methods for the purpose of generating registered images.

Jaderberg et al. [49, 50, 51, 52, 53, 54] introduced spatial transformer networks (STN) to align input images in a larger task-specific network. STNs, however, need many labeled training examples which makes them unsuitable for our application. Sokooti et. al. [7, 55, 56, 57, 58, 59] propose RegNet that uses CNNs trained on simulated deformations to generate displacement vector fields for a pair of unimodal images. Vos et. al. [60, 61, 62, 63, 64, 65] propose the deformable image registration network (DIRNet) which takes pairs of fixed and moving images as input, and outputs a transformed image non-iteratively. Training is completely unsupervised and unlike previous methods it is not trained with known registration transformations. Uzunova et. al. [66, 67, 68, 69, 70, 71] propose to learn representative shape and appearance models from few training samples, and embed them in a new model-based data augmentation scheme to generate huge amounts of ground truth data. Rohe et. al. [72, 73, 74, 75, 76, 77] propose SVF-Net that trains a network using reference deformations obtained by registering *previously segmented* regions of interest (ROIs). Balakrishnan et. al. [6, 78, 79, 80, 81, 82] proposed a CNN based method that learns a parameterized registration function from a collection of training volumes, and does not require ground truth correspondences during training. The above methods are limited by the need of spatially corresponding patches ([7, 60, 83, 84, 85, 86, 87, 88, 89, 90]) or being too dependent on training data.

The above limitations can be overcome to some extent by using generative models that directly generate the registered image and the deformation field. In previous work [91, 92, 93, 94, 95, 96] we used generative adversarial networks (GANs) for multimodal retinal image registration where the trained network outputs the registered image and the deformation field. We show that by incorporating appropriate constraints in the adversarial loss and content loss func-

tion, generative models are fairly reliable in directly generating the registered image and its corresponding deformation field. However, we also observe that GANs tend to misregister local regions with multiple structures. To address this shortcoming, in [8, 97, 98, 99, 100, 101] we propose a joint registration and segmentation method that incorporates segmentation information into the registration process to achieve better registration performance than conventional methods. The segmentation information is integrated as part of the adversarial loss function and experimental results show its significant contribution in improving registration accuracy.

Despite the improvements brought about by joint registration and segmentation in [8, 102, 103, 104, 105, 106], its success depends upon training data with corresponding information about the applied deformation field. Consequently, this restricts its application due to the need for generating images with known deformation field. Previous works have explored different feature spaces for domain independent tasks as in cross modality face detection using deep local descriptors and cross modality enumeration loss [107, 108, 109, 110, 111, 112]. This approach has led to better robustness on traditional datasets. Shang et. al. in [113, 114, 115] propose a unsupervised feature selection algorithm for sparse subspace learning that simultaneously preserves local discriminant structure and local geometric structure. Li et. al. [13] propose auto correlation based local landmark alignment. Yang et. al. in [116] propose an integrated tumor classification framework that addresses problems of small sample and unbalanced datasets using an inverse space sparse representation. With popularity of deep learning methods much focus has also been put on efficient learning approaches such as class specific features [117], asymmetric 3D convolutions [118], and semi-supervised domain adaptation [119], while autoencoders have been used in [120] for simultaneous nucleus detection and feature extraction in histopathology tissue images. To overcome the challenge of transforming medical images to a suitable feature space, we explore a domain adaptation based method that uses a pre-trained network on one type of images to register novel images of another image type.

Compared to our previous works ([91, 8]) this work has the following novelties: 1) we use latent vector representation from convolutional auto encoders in the image registration process; 2) the latent space image is used to generate registered image and the deformation field; 3) the latent feature representation also serves the purpose of domain adaptation wherein a new image pair is easily registered with no network finetuning.

2. Methods

Figure 1 shows the architecture of our proposed method. In the first stage (Figure 1 (a)) two convolutional autoencoders (CAEs) are trained on the reference image (I^{Ref}) and floating image (I^{Flt}). The CAEs are basically tasked with reconstructing the input image through a series of encoding and decoding stages. The output of the encoding stage results in a 2D latent space representation (which we denote as z^{src} and z^{flt} respectively) that is used to reconstruct the original image. The latent space representations act as input to a generative adversarial network (GAN) whose generator network reconstructs the original image (Figure 1 (b)) through a series of convolution and upsampling stages. The output of the generator network is the registered image or transformed image (I^{Trans}) and the recovered deformation field ($I^{Def-Recv}$). The output matrix shape has same number of rows as input image, but twice the number of columns, placing the registered image and deformation field side by side. The first half-image is the registered image while the second half-image is the deformation field. During training the discriminator network (Figure 1 (c)) also comes into play by taking as input I^{Reg} and $I^{Def-Recv}$ and comparing with the ground truth data. The feedback from the discriminator influences the updates of the generator weights. During testing only the generator network is used. The steps for training the registration network is summarized in Algorithm 1, and subsequent steps to obtain a registered image during inference time is summarized in Algorithm 2.

GANs [121] are generative models trained in an adversarial setting. The

generator G outputs a desired image type while discriminator D outputs a probability of the generated image matching the training data. GANs have been used in various applications such as image super resolution [122, 123, 3], image synthesis and image translation using conditional GANs (cGANs) [124, 1, 36] and cyclic GANs (cycleGANs) [125]. In cGANs the output is conditioned on the input image and a random noise vector, and requires training image pairs. On the other hand cycleGANs do not require training image pairs but enforce consistency of deformation field.

Algorithm 1 Training Steps for Registration Network

- 1: **procedure** DOMAIN ADAPTATION BASED IMAGE REGISTRATION
 - 2: $I^{Ref}, I^{Flt} \leftarrow$ Reference and Floating Images
 - 3: $z^{Ref}, z^{Flt} \leftarrow$ convolutional auto encoder outputs for I^{Ref}, I^{Flt}
 - 4: $I^{Def-App} \leftarrow$ actual deformation field between I^{Ref} and I^{Flt}
 - 5: *Training loop:*
 - 6: Input images I^{Ref}, I^{Flt} are fed into the Generator G
 - 7: Auxillary inputs z^{Ref}, z^{Flt} to G
 - 8: Generate intermediate registered image I^{Trans} and recovered deformation field $I^{Def-Recv}$
 - 9: Feed $I^{Trans}, I^{Ref}, I^{Flt}, I^{Def-App}, I^{Def-Recv}$ to discriminator D
 - 10: Calculate $l_{content}$ (Eqn. 2) and L_{adv} (Eqn. 6), and combine to get the full objective function term (Eqn. 7)
 - 11: **close**
 - 12: **Outputs:** Final $UReg - Net$ to output I^{Trans} and $I^{Def-Recv}$
-

2.1. Convolutional Autoencoder Training

Our proposed convolutional auto encoder (CAE) (Figure 1 (a)) takes a 512×512 input image. The first convolution layer has 32 filters of size 3×3 followed by a max pooling layer of subsampling factor 2. This is followed by two more stages of convolution and max pooling layers. The two convolution layers have 64 filters each of 3×3 . Thus the encoder part outputs a $2D$ latent space representation

Algorithm 2 Register Image Pair Using Pre-trained $UReg - Net$

- 1: **procedure** DOMAIN ADAPTATION BASED IMAGE REGISTRATION
 - 2: $I^{Ref}, I^{Flt} \leftarrow$ Reference and Floating Images for registration
 - 3: Obtain $z^{Ref}, z^{Flt} \leftarrow$ CAE outputs for I^{Ref}, I^{Flt}
 - 4: Input z^{Ref}, z^{Flt} to $UReg - Net$
 - 5: Output I^{Trans} and $I^{Def-Recv}$, the registered image and recovered deformation field
 - 6: Calculate registration error between $I^{Def-Recv}$ and $I^{Def-App}$ (if available)
-

of the input image denoted as z of dimension 64×64 . Similarly the decoder has 3 stages of upsampling and deconvolution layers that reconstruct the original image. In the first stage we train the CAE end to end to reconstruct the original image and consequently z is an accurate representation of the input image in the latent space. We train two separate CAEs for I^{Ref} and I^{Flt} . Since we use all convolution layers our network is independent of input image size, and the number of layers in the encoder and decoder part can be varied to suit our training data.

2.2. Generating Registered Images

Figure 1 (b) shows the generator network G . It employs residual blocks, each block having two convolution layers with 3×3 filters and 64 feature maps, followed by batch normalization and ReLU activation. Each convolution layer is followed by a upsampling layer and deconvolution. There are three stages of convolution and upsampling blocks thus restoring the latent space representation back to its original dimension. In addition to generating the registered image I^{Trans} , G also outputs a deformation field $I^{Def-Recv}$.

The training database has chest Xray images of patients with multiple visits. To generate training data each of the images is subjected to various types of local elastic deformation using B-splines with the pixel displacements in the range of $\pm[1, 20]$. The original undistorted image is I^{Ref} and the resulting

deformed images are I^{Flt} . Each I^{Ref} can have multiple I^{Flt} . Applying synthetic deformations allows us to: 1) accurately quantify the registration error between $I^{Def-App}$ and $I^{Def-Recv}$, the applied and recovered deformation fields; and 2) determine the similarity between I^{Trans} and I^{Ref} .

G is a feed-forward CNN whose parameters θ_G are given by,

$$\hat{\theta} = \arg \min_{\theta_G} \frac{1}{N} \sum_{n=1}^N l^{Reg} (G_{\theta_G}(I^{Flt}), I^{Ref}, I^{Flt}), \quad (1)$$

where the registration loss function l^{Reg} combines content loss (Eqn. 2) and adversarial loss (Eqn. 3), and $G_{\theta_G}(I^{Flt}) = I^{Trans}$ the registered image. The content loss is given by

$$l_{content}(I^{Trans}, I^{Ref}) = NMI(I^{Ref}, I^{Trans}) + [1 - SSIM(I^{Ref}, I^{Trans})] + VGG(I^{Ref}, I^{Trans}). \quad (2)$$

NMI denotes normalized mutual information between I^{Ref} and I^{Trans} and is suitable for multimodal and unimodal deformable registration [126]. NMI determines the joint occurrence of intensity pairs for corresponding voxels across an image pair. NMI is robust in accounting for intensity changes and is robust to any intensity distribution differences that may arise due to intensity variations as a result of view point variance. $SSIM$ denotes structural similarity index metric (SSIM) based on edge distribution [127] and quantifies landmark correspondence between different images. $SSIM \in [0, 1]$ with higher values indicating greater similarity. The advantage of SSIM is independence from intensity matching, as it relies on shape matching which is more robust under different conditions.

VGG is the $L2$ distance between two images using all the feature maps obtained from a pre-trained $VGG16$ network [128]. This sums up to $64 \times 2 + 128 \times 2 + 256 \times 2 + 512 \times 3 + 512 \times 3 = 3968$ feature maps. The feature maps are of different dimensions due to multiple max pooling steps. Using all feature maps ensures we are comparing information from multiple scales, both coarse and fine, and thus improves robustness. The feature maps are normalized to have values between $[0, 1]$.

The discriminator D (Figure 1 (c)) has eight convolution layers with the kernels increasing by a factor of 2 from 64 to 512 . Leaky ReLU activation is used and strided convolutions reduce the image dimension when the number of features is doubled. The resulting 512 feature maps are followed by two dense layers and a final sigmoid activation to obtain a probability map. D evaluates similarity of intensity distribution between I^{Trans} and I^{Flt} , and the error between generated and reference deformation fields.

2.3. Deformation Field Consistency

CycleGANs [125] learn mapping functions $G : X \rightarrow Y$ and $F : Y \rightarrow X$, between image sets $X = I^{Flt}$ and $Y = I^{Ref}$. Adversarial discriminators D_X differentiate between images x and registered images $F(y)$, and D_Y distinguishes between y and $G(x)$. G registers I^{Flt} to I^{Ref} while F is trained to register I^{Ref} to I^{Flt} . We refer the reader to [125] for implementation details. In addition to the content loss (Eqn 2) we have: 1) an adversarial loss; and 2) a cycle consistency loss to ensure transformations G, F do not contradict each other.

Adversarial Loss: The adversarial loss is an important component to ensure that the generated outputs are plausible. In previous applications the adversarial loss was based on the similarity of generated image to training data distribution. Since our generator network has multiple outputs we have additional terms for the adversarial loss. The first term matches the distribution of I^{Trans} to I^{Flt} and is given by:

$$L_{cycGAN}(G, D_Y) = E_{y \in p_{data}(y)} [\log D_Y(y)] + E_{x \in p_{data}(x)} [\log (1 - D_Y(G(x)))], \quad (3)$$

We retain notations X, Y for conciseness. There also exists $L_{cycGAN}(F, D_X)$, the corresponding adversarial loss for F and D_X and is given by

$$L_{cycGAN}(F, D_X) = E_{x \in p_{data}(x)} [\log D_X(x)] + E_{y \in p_{data}(y)} [\log (1 - D_X(F(y)))]. \quad (4)$$

Cycle consistency loss ensures that for each $x \in X$ the reverse deformation should bring x back to the original image, i.e. $x \rightarrow G(x) \rightarrow F(G(x)) \approx x$.

Similar constraints also apply for mapping F and y . This is achieved using,

$$L_{cyc}(G, F) = E_x \|F(G(x)) - x\|_1 + E_y \|G(F(y)) - y\|_1, \quad (5)$$

Instead of the original images, I^{Ref} and I^{Flt} , we use their latent vector representations as input to the generator to obtain I^{Trans} .

2.4. Integrating Deformation Field Information

The second component of the adversarial loss is the mean square error between $I^{Def-App}$ and $I^{Def-Recv}$, the applied and recovered deformation fields. The final adversarial loss is

$$L_{adv} = L_{cycGAN}(G, D_{I^{Ref}}) + L_{cycGAN}(F, D_{I^{Flt}}) + \log(1 - MSE_{Norm}(I^{Def-App}, I^{Def-Recv})), \quad (6)$$

where MSE_{Norm} is the MSE normalized to $[0, 1]$, and $1 - MSE_{Norm}$ ensures that similar deformation fields gives a corresponding higher value. Thus all terms in the adversarial loss function have values in $[0, 1]$. The full objective function is given by

$$L(G, F, D_{I^{Flt}}, D_{I^{Ref}}) = L_{adv} + l_{content} + \lambda L_{cyc}(G, F) \quad (7)$$

where $\lambda = 10$ controls the contribution of the two objectives. The optimal parameters are given by:

$$G^*, F^* = \arg \min_{F, G} \max_{D_{I^{Flt}}, D_{I^{Ref}}} L(G, F, D_{I^{Flt}}, D_{I^{Ref}}) \quad (8)$$

2.5. Registering A Test Image

We have trained our image with reference and floating images from the same modality (i.e., chest xray). After training is complete the network weights are such that the generated image is the registered version of I^{Flt} . A notable difference from previous methods [8, 91] is instead of the actual images, the input is a latent space representation of the input image pair. This novelty allows us to register different image types by inputting their embedded representations instead of the actual image. Since the network is not trained on the actual

images it is agnostic to the image type and can be used for different image modalities.

In this work we consider two different test image scenarios: 1) brain MR image registration where the reference and floating images are of the same modality; 2) multimodal retinal image registration where the reference image consists of retinal fundus images and the floating images are fluorescein angiography (FA) images. For brain MRI registration I^{Ref} is each of the brain image slices while I^{Flt} is generated through synthetic deformations. I^{Ref} and I^{Flt} are input through the respective CAEs to obtain z^{Ref} and z^{Flt} . Using the latent space representations the network G is able to generate the I^{Trans} and the deformation field $I^{Def-Recv}$. Since we use all convolution layers our network is independent on the input size.

In the case of multimodal retinal image registration I^{Ref} are the fundus images while the FA images are I^{Flt} . They are put through the corresponding pre-trained CAEs and the output z are input to G to obtain the registered image and deformation field. During the test stage the discriminator network D is not used. The successful registration of multimodal images and organs different from the training data shows that our method is able to achieve domain adaptation in an unsupervised manner.

3. Experiments

3.1. Dataset Description

Our registration method was first validated on the NIH ChestXray14 dataset [129]. The original dataset contains 112,120 frontal-view X-rays with 14 disease labels (multi-labels for each image), which are obtained from associated radiology reports. Since the original dataset is designed for classification studies, we selected samples and applied the following steps to make it suitable for validating registration experiments.

1. 50 patients each from all the 14 disease classes were selected, giving a total of $14 \times 50 = 700$ different patients. Care was taken to ensure that all the

patients had multiple visits (minimum 3 visits and maximum 8 visits).

2. As described previously we take these images as I^{Ref} and generate corresponding floating images by simulating elastic deformations.
3. In total we had 2812 reference images from 700 patients. For each I^{Ref} we generate 20 I^{Flt} to obtain 56240 floating images.
4. For all our experiments we split the dataset into training, validation and test sets comprising of 70, 10, 20% of the images. The split was done at the patient level such that images from a single patient were in one fold only. All the reported results for chest xray images are for the test set.

Validation of registration performance is usually based on the accuracy of landmark alignment before and after registration. Since we had available the applied deformation field we calculate the alignment/overlap error before registration. Successful registration reduces this error. The registration error is quantified by the mean absolute distance (MAD) which measures the average distance between the two set of edge points for an anatomical region. We manually outline the two lungs in some images using which a segmentation overlap measure such as using Dice Metric (DM) is calculated. Alignment accuracy is also determined using the 95% Hausdorff Distance (HD_{95}). An essential objective of registration is to monitor changes of pathology and organ function over time and HD_{95} and DM quantify the overlap of patient segmentation masks from different visits. Lower values of MAD and HD_{95} , and higher values of DM indicate better registration performance.

3.2. Implementation Steps

Our method was implemented in TensorFlow. We use Adam [130] with $\beta_1 = 0.93$ and batch normalization. The generator network G was trained with a learning rate of 0.001 and 10^5 update iterations. Mean square error (MSE) based ResNet was used to initialize G . The final GAN was trained with 10^5 update iterations at learning rate 10^{-3} . Training and test was performed on a NVIDIA Tesla K40 GPU with 12 GB RAM.

We show results for: 1) *UReg – Net*: - our proposed unsupervised registration network; 2) *URegImage*: - *UReg – Net* without using the latent space feature z but the original image; 3) *FlowNet*: - the registration method of [43]; 4) *DIRNet*: - the method of [60]; 5) *JRS – Net*: - the joint registration and segmentation network using GANs ([8]); 6) *Voxel Morph*: - the registration method of [6]; and 7) a conventional registration method Elastix [131].

Note that only localized deformations were simulated and hence we do not perform any affine alignment before using the different methods. The average training time for the augmented dataset with 56240 images is 30 hours. The following parameter settings were used for Elastix: non rigid registration using normalized mutual information (NMI) as the cost function. Nonrigid transformations are modelled by B-splines [126], embedded in a multi-grid setting. The grid spacing was set to 80, 40, 20, 10, 5 mm with the corresponding downsampling factors being 4, 3, 2, 1, 1.

3.3. Chest XRay Image Registration Results

In this section we show results when the trained network is applied on a separate test set of chest xray images consisting of I^{Ref} and I^{Flt} obtained by synthetic deformations. Registration results of the lung for normal and diseased cases are summarized in Tables 1,2. We observe that the performance is similar for the two kinds of images thus demonstrating that our method is equally effective for diseased and normal images.

Figure 2 shows results for a non-diseased image. Figure 2 (a) shows I^{Flt} and Figure 2 (b) shows the superimposed segmentation masks of I^{Ref} (I_{Seg}^{Ref}) and I^{Flt} (I_{Seg}^{Flt}) on the reference image to give an idea of the degree of misalignment before registration. Figures 2 (c)-(f) show the superimposed contours after registration using different methods. In these examples I_{Seg}^{Trans} is shown in green with I_{Seg}^{Ref} in red. I_{Seg}^{Trans} is obtained by applying the recovered deformation field to I_{Seg}^{Flt} . Better registration is indicated by closer alignment of the two contours. Figure 3 shows the corresponding results for the diseased case.

	Normal Images			
	Bef.	After Registration		
	Reg	UReg-Net	UReg _{Image}	DIRNet
DM(%)	78.9	89.3	85.2	84.8
HD ₉₅ (mm)	12.9	6.9	8.4	8.7
MAD	13.7	7.3	8.9	9.1
Time(s)		0.5	0.4	0.6
	After Registration			
	FlowNet	JRS-Net	Elastix	VoxelMorph
DM(%)	83.5	88.6	82.1	88.2
HD ₉₅ (mm)	9.8	7.5	10.8	7.4
MAD	13.7	8.6	11.1	7.9
Time(s)	0.5	0.6	21	0.6

Table 1: Image registration results for **left and right lung** using different methods on **non-diseased images** of the NIH-14 database. *Time* indicates computation time in seconds.

3.4. Accuracy of Generated Images

Our method is different from previous image registration approaches since we directly generate the registered image instead of iteratively updating the image. Consequently, there is always a risk that the images generated by the GAN may not be realistic or the generated images are not diverse enough. To ensure that it is not the case we perform a classification experiment.

We take a VGG-16 classifier [128] pre-trained on the ImageNet dataset [132] and use 700 reference images, with data augmentation, to finetune it for a 14 label classification problem which is the number of diseased classes represented in the NIH dataset. The finetuning is done under a 5– fold cross validation setting to get an average area under curve (AUC) of 82.5 for the 14 class disease classification problem. This value is the baseline against which other results are compared.

After finetuning, the classifier is evaluated on the test set of 2112 floating

	Diseased Images			
	Bef.	After Registration		
	Reg	UReg-Net	UReg _{Image}	DIRNet
DM(%)	79.1	88.9	85.0	84.4
HD ₉₅ (mm)	11.8	7.3	8.6	8.9
MAD	12.7	7.9	9.2	9.6
Time(s)		0.5	0.4	0.6
	After Registration			
	FlowNet	JRS-Net	Elastix	Voxel Morph
DM(%)	83.1	88.2	81.5	87.9
HD ₉₅ (mm)	10.1	8.1	11.5	8.0
MAD	12.7	9.0	12.1	8.3
Time(s)	0.5	0.3	21	0.6

Table 2: Image registration results for **left and right lung** using different methods on diseased images of the NIH-14 database. *Time* indicates computation time in seconds.

images and the corresponding registered images generated by the registration GAN. If the generated images are real then the classification performance on the generated images would be similar to the baseline. The AUC values obtained for classifying the generated images was 81.9 and 82.8, respectively, for the real floating images and registered images generated by the GAN. The two very similar values and their closeness to the baseline demonstrate that the generated images have a high degree of realism.

In another set of experiments we used a random noise vector instead of the latent vector from the auto encoder. The generated images are used to repeat the classification experiment as described above. We obtain AUC values of 76.2 with the VGG classifier, which is a significant decrease from the performance of latent vector encoding. The corresponding p-value from a t-test is 0.032, indicating statistically different results and reinforce the fact that any arbitrary vector is not suitable for domain independent registration. Rather it is the

use of CAEs that transforms the image to a latent feature space and exhibits enhanced performance through the generation of realistic images.

Furthermore, in another set of experiments we take the output of the CAEs and add small amounts of Gaussian noise (zero mean and $\sigma \in [0.21]$) to distort the latent feature vector. The corresponding classification experiment results in AUC values of 81.1, with $p > 0.0754$ compared to the previously mentioned baseline. These results show our CAE based approach is fairly robust and, despite added noise, is able to generate realistic images.

3.5. Ablation Study Experiments

Equations 2,6 denote the different terms used in the cost function. In this section we describe a set of experiments that evaluate the importance of different sources of information in achieving registration. Equation 2 has NMI, VGG and SSIM terms. In one set of experiments we exclude the NMI term in the cost function and evaluate the images thus generated. The method is denoted as $UReg_w-NMI$, or $UReg-Net$ without NMI. We also generate results without VGG ($UReg_w-VGG$) and SSIM ($UReg_w-SSIM$) terms in Equation 2, and by excluding deformation field error, $\log(1 - MSE_{Norm}(I^{Def-App}, I^{Def-Recv}))$, in Eqn. 6 ($UReg_w-Def$).

Results of ablation study experiments on diseased and normal images are summarized in Tables 3,4. The performance drops by a statistically significant measure when we exclude different terms of the cost function. Of particular importance are the numbers for $UReg_{Image}$ that show the maximum drop in performance compared to $UReg-Net$. This clearly demonstrates the advantage of using latent space representation instead of images for registration.

3.6. Validation of Synthetic Images By Clinical Experts

We also validate the authenticity of generated images through visual examination by clinical experts. A 90 minutes session was set with three experienced radiologists each having over 15 years of experience in the diagnosis of lung conditions from X-ray/CT images. They are tasked with providing feedback

	Bef.	After Registration	
	Reg	UReg _{Image}	UReg _{w-NMI}
DM(%)	78.9	85.2	83.4
HD ₉₅ (mm)	12.9	8.4	8.9
MAD(mm)	13.7	8.9	9.5
Time(s)		0.4	0.4
	After Registration		
	UReg _{w-VGG}	UReg _{w-SSIM}	UReg _{w-Def}
DM(%)	81.9	82.6	82.1
HD ₉₅ (mm)	9.9	9.2	10.1
MAD(mm)	13.7	9.8	10.9
Time(s)	0.4	0.4	0.4

Table 3: Image registration results for normal images by excluding different terms in the cost function. *Time* indicates computation time in seconds.

whether the generated registered images and their deformation fields are realistic or not. 150 reference and floating image pairs are selected, and registered images registered using three different approaches: 1) conventional image registration using Elastix; 2) GAN based registration using the original images (GAN_{Image}); and 3) our GAN based registration method using latent vector representations of the images as input (GAN_Z). For 2) we re-trained our network, replacing z with images. The selected images had a uniform distribution amongst the 14 disease classes. For each case the I^{Ref} and I^{Flt} were first displayed to all three radiologists, followed by the display of I^{Trans} and $I^{Def-Recv}$. The experts were asked to indicate whether I^{Trans} is realistic or not, and were agnostic to the method that produced the registered images. Each expert viewed all registered images obtained by each of the three methods.

The results for consensus on realism is summarized in Table 5. The results of Elastix based registration act as a baseline and, expectedly, have high agreement on realism since there are no generative models involved. The few images that

	Bef.	After Registration	
	Reg	UReg _{Image}	UReg _{w-NMI}
DM(%)	79.1	85.0	83.2
HD ₉₅ (mm)	11.8	8.6	9.3
MAD(mm)	12.7	9.2	9.8
Time(s)		0.4	0.4
	After Registration		
	UReg _{w-VGG}	UReg _{w-SSIM}	UReg _{w-Def}
DM(%)	82.0	82.3	81.8
HD ₉₅ (mm)	10.4	9.1	10.3
MAD(mm)	11.2	10.1	11.1
Time(s)	0.4	0.4	0.4

Table 4: Image registration results for diseased images by excluding different terms in the cost function. *Time* indicates computation time in seconds.

are deemed as unrealistic are, possibly, a result of inaccurate registration. For GAN_{Image} the agreement drops by about 4 – 5%. This is not unexpected and has to do with the capacity of the implemented GAN model for learning desired image distributions. In the case of GAN_Z the agreement drops slightly by 1 – 1.5%. Although it indicates a reduced ability to generate realistic images, the difference with respect to GAN_{Image} is not significant as indicated by a p-value of 0.0867. Thus we can conclude that use of latent vector representations does not significantly degrade the realism of generated images. But it provides the advantage of using the registration method for multiple problem domains without laborious retraining.

3.7. Atlas Registration Results Using Brain MRI

We demonstrate our method on the task of brain MRI registration. We used the 800 images of the ADNI-1 dataset [133] consisting of 200 controls, 400 MCI and 200 Alzheimer’s Disease patients. The MRI protocol for ADNI1 focused on consistent longitudinal structural imaging on 1.5T scanners using T1 and

Agreement Statistics	Registration Method		
	Elastix	GAN_{Image}	GAN_Z
All 3 Experts	91.3 (137)	84.7 (127)	83.4 (125)
Atleast 2 Experts	94.0 (141)	87.3 (131)	85.3 (128)
Atleast 1 Expert	98.7 (148)	89.3 (134)	87.3 (131)
No Experts	1.3 (2)	10.7 (16)	12.7 (19)

Table 5: Agreement statistics for different registration methods amongst 3 radiologists. Numbers in bold indicate percentage of agreement among clinicians while numbers within brackets indicate actual numbers out of 150 patients.

dual echo $T2$ -weighted sequences. All scans were resampled to $256 \times 256 \times 256$ with 1mm isotropic voxels. Pre-processing includes affine registration and brain extraction using FreeSurfer [134], and cropping the resulting images to $160 \times 192 \times 224$. The dataset is split into 560, 120, and 120 volumes for training, validation, and testing. We simulate elastic deformations to generate the floating images using which we evaluate registration performance. Registration performance was calculated for 2D slices.

Figure 4 shows results for image registration. We show the reference image (or the atlas image) in Figure 4 (a) followed by an example floating image in Figure 4 (b). The ventricle structure to be aligned is shown in red in both images. Similar to the results of lung images, Figure 4 (c)-(i) show the deformed structures obtained by applying the registration field obtained from different methods to the floating image and superimposing these structures on the atlas image. The deformed structures from the floating image are shown in green. In case of a perfect registration the green and red contours should coincide perfectly. Table 6 shows the results of atlas image based brain registration using the average Dice scores between structures before and after registration.

3.8. Performance on New Test Images

So far we have shown results where the training and test set were of the same anatomies (i.e., lung to lung and brain to brain). In this section we show results

	Bef.	After Registration		
	Reg	URegNet	URegImage	DIRNet
DM(%)	67.2	78.5	74.6	75.1
HD ₉₅ (mm)	14.5	9.4	11.1	11.4
MAD	16.1	10.5	12.1	12.7
Time(s)		0.5	0.4	0.6
	After Registration			
	FlowNet	JRS-Net	Elastix	VoxelMorph
DM(%)	73.2	76.8	73.1	74.9
HD ₉₅ (mm)	12.6	11.8	13.8	11.9
MAD	13.9	13.1	15.0	12.8
Time(s)	0.5	0.6	21	0.5

Table 6: Atlas based registration results for different methods on brain images.

for cases where the training was performed with one image type and used to register images of the other type. Table 7 summarizes the performance of all the deep learning networks when trained on the diseased lung images and used to register brain images, while Table 8 summarizes performance when the networks were trained on brain images and used to register diseased lung images. Compared to the results for lung (Table 2) and brain (Table 6) images, it is obvious that for the same type of training and test images registration performance is much better than having different training and test images. Despite these limitations our proposed method, *UReg-Net*, performs better than other methods and the values are close to the case of having same train and test image. Note that the Elastix method does not involve learning and acts as a baseline, while other methods are trained on images different from the test images

3.9. Retinal Image Registration Results

The dataset consists of retinal colour fundus images and fluorescein angiography (FA) images obtained from 30 normal subjects. Both images are 576×720 pixels and fovea centred [135]. Registration ground truth was developed using

	Bef.	After Registration		
	Reg	UReg-Net	UReg _{Image}	DIRNet
DM(%)	67.2	74.1	71.2	70.9
HD ₉₅ (mm)	14.5	10.8	12.3	12.7
MAD	16.1	12.0	13.6	14.1
Time(s)		0.5	0.4	0.6
	After Registration			
	FlowNet	JRS-Net	Elastix	VoxelMorph
DM(%)	69.4	72.2	71.1	71.3
HD ₉₅ (mm)	13.1	13.8	14.2	13.6
MAD	15.1	14.6	15.9	14.2
Time(s)	0.5	0.6	21	0.5

Table 7: Registration results for brain images when network is trained on diseased lung images.

the Insight Toolkit (ITK). The Frangi vesselness[136] feature was utilised to find the vasculature, and the maps were aligned using sum of squared differences (SSD). Three out of 30 images could not be aligned due to poor contrast and one FA image was missing, leaving us with a final set of 26 registered pairs. We use the fundus images as I^{Ref} and generate floating images from the FA images by simulating different deformations (using SimpleITK) such as rigid, affine and elastic deformations(maximum displacement of a pixel was ± 10 mm. 1500 sets of deformations were generated for each image pair giving a total of 39000 image pairs to be evaluated for registration performance.

Our algorithm’s performance was evaluated using previously mentioned metrics. Before applying simulated deformation the mean Dice overlap of the vasculature between the fundus and FA images across all 26 patients is 99.2, which indicates highly accurate alignment. After simulating deformations the individual Dice overlap reduces considerably depending upon the extent of deformation. The Dice value after successful registration is expected to be higher than before registration. We also calculate the 95 percentile Hausdorff Distance (HD_{95}) and

	Diseased Images			
	Bef.	After Registration		
	Reg	UReg-Net	UReg _{Image}	DIRNet
DM(%)	79.1	84.6	82.0	82.1
HD ₉₅ (mm)	11.8	8.8	10.0	10.3
MAD	12.7	9.5	10.8	10.9
Time(s)		0.5	0.4	0.6
	Diseased Images			
	After Registration			
	FlowNet	JRS-Net	Elastix	VoxelMorph
DM(%)	81.7	83.1	81.6	82.5
HD ₉₅ (mm)	9.9	11.1	11.6	10.2
MAD	12.3	11.6	13.1	11.6
Time(s)	0.5	0.4	21	0.6

Table 8: Registration results for diseased lung images when network is trained on brain images.

the mean absolute surface distance (MAD) before and after registration. We calculate the mean square error (MSE) between the registered FA image and the original undeformed FA image to quantify their similarity. The intensity of both images was normalized to lie in $[0, 1]$.

In this scenario all the deep learning networks were trained on the chest xray images and used to register the retinal image pairs. Table 9 shows the registration performance for the different methods. Figure 5 shows registration results for retinal images. It is observed (for retinal, lung and brain image registration) that the deep learning methods perform better than Elastix for same training and test images but are not significantly different for different train and test pairs, except for *UReg - Net* which is designed to overcome this challenge. Thus our approach of using latent space feature maps is highly effective in achieving accurate registration on new test images.

	Bef.	After Registration		
	Reg	UReg-Net	UReg _{Image}	DIRNet
DM(%)	72.5	83.9	81.8	81.3
HD ₉₅ (mm)	12.7	9.6	10.9	11.2
MAD	13.4	10.2	11.6	11.8
Time(s)		0.3	0.3	0.4
	After Registration			
	FlowNet	JRS-Net	Elastix	VoxelMorph
DM(%)	81.1	82.1	81.1	81.7
HD ₉₅ (mm)	10.7	11.9	12.5	10.9
MAD	13.1	12.4	14.1	12.2
Time(s)	0.3	0.6	18	0.4

Table 9: Registration results for retinal images when network is trained on chest xray images.

4. Discussions

The images generated by our method exhibit a high degree of realism. Although GANs have their limitations in image generation, our approach produces satisfactory results in most cases as supported by the agreement statistics in Table 5. We hypothesize that imposing very specific constraints during model training by adding cost terms, although narrowing the search space, may contribute to more realistic images since the network is trained to generate images satisfying very specific criteria. However this is realizable only in the presence of sufficient training data. In future work we aim to investigate this hypothesis which could lead to a better understanding of GAN training.

The latent space representation contributes towards more accurate registration by learning the most effective representation of the image. Medical images have lower dimension and resolution than natural images and hence provide less information. Consequently a lower dimensional representation, as in the case of latent space representation, contributes in improving registration performance by guiding the network to focus on most informative and discriminative regions.

If we add another convolution and max pooling layer such that the latent feature map is 32×32 we observe a drop in registration accuracy. On the other hand if the latent feature map is 128×128 , there is no significant improvement in registration performance but increases the training time by nearly 6 times. Hence we choose to use the 64×64 maps as the optimal representation.

While our method does improve on existing methods, we also observe a few failure cases. One common scenario is when the floating image has multiple disease labels. Although our method is not dependent on the disease label, multiple labels indicate presence of multiple pathologies and hence the images are hazy in appearance. Consequently, the registration output is not accurate as multiple pathologies distort the discriminative information that can be extracted from the image. In such scenarios using the original images instead of latent feature maps does not make much difference to the result. Although we demonstrate that the network trained on Xray images can register retinal images, the results can be much improved if the training and test imaging modality are similar. These observations motivate us to explore other image feature representation methods such that the common feature space is equally informative and discriminative irrespective of the input images.

5. Conclusion

We have proposed a novel deep learning framework for registration of different types of medical images using unsupervised domain adaptation and generative adversarial networks. Our proposed method achieves dataset independent registration where it is trained on one kind of images and achieves state of the art performance in registering different image types. GANs are trained to generate the registered image and the corresponding deformation field. The primary novelty of our method is the use of latent space feature maps from autoencoders that facilitates dataset independent registration. Experimental results show our domain adaptation based registration method performs better than existing methods that rely on vast amounts of training data for image registration.

On the one hand CAE feature maps lead to better registration by reducing the input feature dimension, while on the other hand they also open up other research questions related to GAN training and image feature representation. We hope to address these questions in future work.

References

- [1] B. Bozorgtabar, D. Mahapatra, H. von Teng, A. Pollinger, L. Ebner, J.-P. Thiran, M. Reyes, Informative sample generation using class aware generative adversarial networks for classification of chest xrays., *Computer Vision and Image Understanding* 184 (2019) 57–65 (2019).
- [2] D. Mahapatra, Z. Ge, Training data independent image registration using generative adversarial networks and domain adaptation., *In press Pattern Recognition* 100 (2020) 1–14 (2020).
- [3] D. Mahapatra, B. Bozorgtabar, R. Garnavi, Image super-resolution using progressive generative adversarial networks for medical image analysis., *Computerized Medical Imaging and Graphics* 71 (2019) 30–39 (2019).
- [4] D. Mahapatra, Semi-supervised learning and graph cuts for consensus based medical image segmentation., *Pattern Recognition* 63 (1) (2017) 700–709 (2017).
- [5] J. Zilly, J. Buhmann, D. Mahapatra, Glaucoma detection using entropy sampling and ensemble learning for automatic optic cup and disc segmentation., *In Press Computerized Medical Imaging and Graphics* 55 (1) (2017) 28–41 (2017).
- [6] G. Balakrishnan, A. Zhao, M. Sabuncu, J. Guttag, An supervised learning model for deformable medical image registration, in: *Proc. CVPR*, 2018, pp. 9252–9260 (2018).

- [7] H. Sokooti, B. de Vos, F. Berendsen, B. Lelieveldt, I. Isgum, M. Staring, Nonrigid image registration using multiscale 3d convolutional neural networks, in: MICCAI, 2017, pp. 232–239 (2017).
- [8] D. Mahapatra, Z. Ge, S. Sedai, R. Chakravorty, Joint registration and segmentation of xray images using generative adversarial networks, in: MICCAI-MLMI, 2018, pp. 73–80 (2018).
- [9] Z. Ge, D. Mahapatra, X. Chang, Z. Chen, L. Chi, H. Lu, Improving multi-label chest x-ray disease diagnosis by exploiting disease and health labels dependencies., In press Multimedia Tools and Application (2019) 1–14 (2019).
- [10] D. Mahapatra, F. Vos, J. Buhmann, Active learning based segmentation of crohns disease from abdominal mri., Computer Methods and Programs in Biomedicine 128 (1) (2016) 75–85 (2016).
- [11] D. Mahapatra, J. Buhmann, Visual saliency based active learning for prostate mri segmentation., SPIE Journal of Medical Imaging 3 (1) (2016).
- [12] D. Mahapatra, Combining multiple expert annotations using semi-supervised learning and graph cuts for medical image segmentation., Computer Vision and Image Understanding 151 (1) (2016) 114–123 (2016).
- [13] Z. Li, D. Mahapatra, J. Tielbeek, J. Stoker, L. van Vliet, F. Vos, Image registration based on autocorrelation of local structure., IEEE Trans. Med. Imaging 35 (1) (2016) 63–75 (2016).
- [14] P. Falez, P. Tirilly, I. Bilasco, P. Devienne, P. Boulet, Unsupervised visual feature learning with spike-timing-dependent plasticity: How far are we from traditional feature learning approaches?., Pattern Recognition 93 (2019) 418–429 (2019).
- [15] D. Mahapatra, Automatic cardiac segmentation using semantic information from random forests., J. Digit. Imaging. 27 (6) (2014) 794–804 (2014).

- [16] D. Mahapatra, S. Gilani, M. Saini., Coherency based spatio-temporal saliency detection for video object segmentation., *IEEE Journal of Selected Topics in Signal Processing*. 8 (3) (2014) 454–462 (2014).
- [17] B. Bozorgtabar, D. Mahapatra, J.-P. Thiran, Exprada: Adversarial domain adaptation for facial expression analysis., *In Press Pattern Recognition* 100 (2020) 15–28 (2020).
- [18] D. Mahapatra, J. Buhmann, Analyzing training information from random forests for improved image segmentation., *IEEE Trans. Imag. Proc.* 23 (4) (2014) 1504–1512 (2014).
- [19] D. Mahapatra, J. Buhmann, Prostate mri segmentation using learned semantic knowledge and graph cuts., *IEEE Trans. Biomed. Engg.* 61 (3) (2014) 756–764 (2014).
- [20] J. maintz, M. Viergever, A survey of medical image registration, *Med. Imag. Anal* 2 (1) (1998) 1–36 (1998).
- [21] D. Mahapatra, J.Tielbeek, J. Makanyanga, J. Stoker, S. Taylor, F. Vos, J. Buhmann, Automatic detection and segmentation of crohn’s disease tissues from abdominal mri., *IEEE Trans. Med. Imaging* 32 (12) (2013) 1232–1248 (2013).
- [22] D. Mahapatra, J.Tielbeek, F. Vos, J. Buhmann, A supervised learning approach for crohn’s disease detection using higher order image statistics and a novel shape asymmetry measure., *J. Digit. Imaging* 26 (5) (2013) 920–931 (2013).
- [23] D. Mahapatra, Cardiac mri segmentation using mutual context information from left and right ventricle., *J. Digit. Imaging* 26 (5) (2013) 898–908 (2013).
- [24] D. Mahapatra, Cardiac image segmentation from cine cardiac mri using graph cuts and shape priors., *J. Digit. Imaging* 26 (4) (2013) 721–730 (2013).

- [25] D. Mahapatra, Joint segmentation and groupwise registration of cardiac perfusion images using temporal information., *J. Digit. Imaging* 26 (2) (2013) 173–182 (2013).
- [26] G. Wu, M. Kim, Q. Wang, B. C. Munsell, , D. Shen., Scalable high performance image registration framework by unsupervised deep feature representations learning., *IEEE Trans. Biomed. Engg.* 63 (7) (2016) 1505–1516 (2016).
- [27] D. Mahapatra, Skull stripping of neonatal brain mri: Using prior shape information with graphcuts., *J. Digit. Imaging* 25 (6) (2012) 802–814 (2012).
- [28] D. Mahapatra, Y. Sun, Integrating segmentation information for improved mrf-based elastic image registration., *IEEE Trans. Imag. Proc.* 21 (1) (2012) 170–183 (2012).
- [29] D. Mahapatra, Y. Sun, Mrf based intensity invariant elastic registration of cardiac perfusion images using saliency information, *IEEE Trans. Biomed. Engg.* 58 (4) (2011) 991–1000 (2011).
- [30] D. Mahapatra, Y. Sun, Rigid registration of renal perfusion images using a neurobiology based visual saliency model, *EURASIP Journal on Image and Video Processing.* (2010) 1–16 (2010).
- [31] S. Miao, Y. Z. Z.J. Wang, R. Liao, Real-time 2d/3d registration via cnn regression, in: *IEEE ISBI*, 2016, pp. 1430–1434 (2016).
- [32] S. Kuanar, V. Athitsos, D. Mahapatra, K. Rao, Z. Akhtar, D. Dasgupta, Low dose abdominal ct image reconstruction: An unsupervised learning based approach, in: *In Proc. IEEE ICIP*, 2019, pp. 1351–1355 (2019).
- [33] B. Bozorgtabar, M. S. Rad, D. Mahapatra, J.-P. Thiran, Syndemo: Synergistic deep feature alignment for joint learning of depth and ego-motion, in: *In Proc. IEEE ICCV*, 2019 (2019).

- [34] Y. Xing, Z. Ge, R. Zeng, D. Mahapatra, J. Seah, M. Law, T. Drummond, Adversarial pulmonary pathology translation for pairwise chest x-ray data augmentation, in: In Proc. MICCAI, 2019, pp. 757–765 (2019).
- [35] D. Mahapatra, Z. Ge, Training data independent image registration with gans using transfer learning and segmentation information, in: In Proc. IEEE ISBI, 2019, pp. 709–713 (2019).
- [36] D. Mahapatra, S. Bozorgtabar, J.-P. Thiran, M. Reyes, Efficient active learning for image classification and segmentation using a sample selection and conditional generative adversarial network, in: In Proc. MICCAI (2), 2018, pp. 580–588 (2018).
- [37] R. Liao, S. Miao, P. de Tournemire, S. Grbic, A. Kamen, T. Mansi, D. Comaniciu, An artificial agent for robust image registration, in: AAAI, 2017, pp. 4168–4175 (2017).
- [38] D. Mahapatra, Z. Ge, S. Sedai, R. Chakravorty., Joint registration and segmentation of xray images using generative adversarial networks, in: In Proc. MICCAI-MLMI, 2018, pp. 73–80 (2018).
- [39] S. Sedai, D. Mahapatra, B. Antony, R. Garnavi, Joint segmentation and uncertainty visualization of retinal layers in optical coherence tomography images using bayesian deep learning, in: In Proc. MICCAI-OMIA, 2018, pp. 219–227 (2018).
- [40] S. Sedai, D. Mahapatra, Z. Ge, R. Chakravorty, R. Garnavi, Deep multi-scale convolutional feature learning for weakly supervised localization of chest pathologies in x-ray images, in: In Proc. MICCAI-MLMI, 2018, pp. 267–275 (2018).
- [41] D. Mahapatra, B. Antony, S. Sedai, R. Garnavi, Deformable medical image registration using generative adversarial networks, in: In Proc. IEEE ISBI, 2018, pp. 1449–1453 (2018).

- [42] S. Sedai, D. Mahapatra, S. Hewavitharanage, S. Maetschke, R. Garnavi, Semi-supervised segmentation of optic cup in retinal fundus images using variational autoencoder,, in: In Proc. MICCAI, 2017, pp. 75–82 (2017).
- [43] A. Dosovitskiy, P. Fischer, et. al., Flownet: Learning optical flow with convolutional networks, in: In Proc. IEEE ICCV, 2015, pp. 2758–2766 (2015).
- [44] D. Mahapatra, S. Bozorgtabar, S. Hewavitahranage, R. Garnavi, Image super resolution using generative adversarial networks and local saliency maps for retinal image analysis,, in: In Proc. MICCAI, 2017, pp. 382–390 (2017).
- [45] P. Roy, R. Tennakoon, K. Cao, S. Sedai, D. Mahapatra, S. Maetschke, R. Garnavi, A novel hybrid approach for severity assessment of diabetic retinopathy in colour fundus images,, in: In Proc. IEEE ISBI, 2017, pp. 1078–1082 (2017).
- [46] P. Roy, R. Chakravorty, S. Sedai, D. Mahapatra, R. Garnavi, Automatic eye type detection in retinal fundus image using fusion of transfer learning and anatomical features, in: In Proc. DICTA, 2016, pp. 1–7 (2016).
- [47] R. Tennakoon, D. Mahapatra, P. Roy, S. Sedai, R. Garnavi, Image quality classification for dr screening using convolutional neural networks, in: In Proc. MICCAI-OMIA, 2016, pp. 113–120 (2016).
- [48] S. Sedai, P. Roy, D. Mahapatra, R. Garnavi, Segmentation of optic disc and optic cup in retinal images using coupled shape regression, in: In Proc. MICCAI-OMIA, 2016, pp. 1–8 (2016).
- [49] M. Jaderberg, K. Simonyan, A. Zisserman, K. Kavukcuoglu, Spatial transformer networks, in: NIPS, 2015, pp. – (2015).
- [50] D. Mahapatra, P. Roy, S. Sedai, R. Garnavi, Retinal image quality classification using saliency maps and cnns, in: In Proc. MICCAI-MLMI, 2016, pp. 172–179 (2016).

- [51] S. Sedai, P. Roy, D. Mahapatra, R. Garnavi, Segmentation of optic disc and optic cup in retinal fundus images using shape regression, in: In Proc. EMBC, 2016, pp. 3260–3264 (2016).
- [52] D. Mahapatra, P. Roy, S. Sedai, R. Garnavi, A cnn based neurobiology inspired approach for retinal image quality assessment, in: In Proc. EMBC, 2016, pp. 1304–1307 (2016).
- [53] J. Zilly, J. Buhmann, D. Mahapatra, Boosting convolutional filters with entropy sampling for optic cup and disc image segmentation from fundus images, in: In Proc. MLMI, 2015, pp. 136–143 (2015).
- [54] D. Mahapatra, J. Buhmann, Visual saliency based active learning for prostate mri segmentation, in: In Proc. MLMI, 2015, pp. 9–16 (2015).
- [55] D. Mahapatra, J. Buhmann, Obtaining consensus annotations for retinal image segmentation using random forest and graph cuts, in: In Proc. OMIA, 2015, pp. 41–48 (2015).
- [56] D. Mahapatra, J. Buhmann, A field of experts model for optic cup and disc segmentation from retinal fundus images, in: In Proc. IEEE ISBI, 2015, pp. 218–221 (2015).
- [57] D. Mahapatra, Z. Li, F. Vos, J. Buhmann, Joint segmentation and group-wise registration of cardiac dce mri using sparse data representations, in: In Proc. IEEE ISBI, 2015, pp. 1312–1315 (2015).
- [58] D. Mahapatra, F. Vos, J. Buhmann, Crohn’s disease segmentation from mri using learned image priors, in: In Proc. IEEE ISBI, 2015, pp. 625–628 (2015).
- [59] H. Kuang, B. Guthier, M. Saini, D. Mahapatra, A. E. Saddik, A real-time smart assistant for video surveillance through handheld devices., in: In Proc. ACM Intl. Conf. Multimedia, 2014, pp. 917–920 (2014).

- [60] B. de Vos, F. Berendsen, M. Viergever, M. Staring, I. Isgum, End-to-end unsupervised deformable image registration with a convolutional neural network, in: MICCAI International Workshop on Deep Learning in Medical Image Analysis, 2017, pp. 204–212 (2017).
- [61] D. Mahapatra, J. Tielbeek, J. Makanyanga, J. Stoker, S. Taylor, F. Vos, J. Buhmann, Combining multiple expert annotations using semi-supervised learning and graph cuts for crohn’s disease segmentation, in: In Proc: MICCAI-ABD, 2014 (2014).
- [62] P. Schüffler, D. Mahapatra, J. Tielbeek, F. Vos, J. Makanyanga, D. Pends, C. Nio, J. Stoker, S. Taylor, J. Buhmann, Semi automatic crohns disease severity assessment on mr imaging, in: In Proc: MICCAI-ABD, 2014 (2014).
- [63] D. Mahapatra, J. Tielbeek, J. Makanyanga, J. Stoker, S. Taylor, F. Vos, J. Buhmann, Active learning based segmentation of crohn’s disease using principles of visual saliency, in: Proc. IEEE ISBI, 2014, pp. 226–229 (2014).
- [64] D. Mahapatra, P. Schüffler, J. Tielbeek, F. Vos, J. Buhmann, Semi-supervised and active learning for automatic segmentation of crohn’s disease, in: Proc. MICCAI, Part 2, 2013, pp. 214–221 (2013).
- [65] P. Schüffler, D. Mahapatra, J. Tielbeek, F. Vos, J. Makanyanga, D. Pends, C. Nio, J. Stoker, S. Taylor, J. Buhmann, A model development pipeline for crohns disease severity assessment from magnetic resonance images, in: In Proc: MICCAI-ABD, 2013 (2013).
- [66] H. Uzunova, M. Wilms, H. Handels, J. Ehrhardt, Training cnns for image registration from few samples with model-based data augmentation, in: In Proc. MICCAI, 2017, pp. 223–231 (2017).
- [67] D. Mahapatra, Graph cut based automatic prostate segmentation using

- learned semantic information, in: Proc. IEEE ISBI, 2013, pp. 1304–1307 (2013).
- [68] D. Mahapatra, J. Buhmann, Automatic cardiac rv segmentation using semantic information with graph cuts, in: Proc. IEEE ISBI, 2013, pp. 1094–1097 (2013).
- [69] D. Mahapatra, J. Tielbeek, F. Vos, J. Buhmann, Weakly supervised semantic segmentation of crohn’s disease tissues from abdominal mri, in: Proc. IEEE ISBI, 2013, pp. 832–835 (2013).
- [70] D. Mahapatra, J. Tielbeek, F. Vos, J. B. ., Crohn’s disease tissue segmentation from abdominal mri using semantic information and graph cuts, in: Proc. IEEE ISBI, 2013, pp. 358–361 (2013).
- [71] D. Mahapatra, J. Tielbeek, F. Vos, J. Buhmann, Localizing and segmenting crohn’s disease affected regions in abdominal mri using novel context features, in: Proc. SPIE Medical Imaging, 2013 (2013).
- [72] M. Rohe, M. Datar, T. Heimann, M. Sermesant, X. Pennec, SVF-Net: Learning deformable image registration using shape matching, in: In Proc.MICCAI, 2017, pp. 266–274 (2017).
- [73] D. Mahapatra, J. Tielbeek, J. Buhmann, F. Vos, A supervised learning based approach to detect crohn’s disease in abdominal mr volumes, in: Proc. MICCAI workshop Computational and Clinical Applications in Abdominal Imaging(MICCAI-ABD), 2012, pp. 97–106 (2012).
- [74] D. Mahapatra, Cardiac lv and rv segmentation using mutual context information, in: Proc. MICCAI-MLMI, 2012, pp. 201–209 (2012).
- [75] D. Mahapatra, Landmark detection in cardiac mri using learned local image statistics, in: Proc. MICCAI-Statistical Atlases and Computational Models of the Heart. Imaging and Modelling Challenges (STACOM), 2012, pp. 115–124 (2012).

- [76] F. M. Vos, J. Tielbeek, R. Naziroglu, Z. Li, P. Schüffler, D. Mahapatra, A. Wiebel, C. Lavini, J. Buhmann, H. Hege, J. Stoker, L. van Vliet, Computational modeling for assessment of IBD: to be or not to be?, in: Proc. IEEE EMBC, 2012, pp. 3974–3977 (2012).
- [77] D. Mahapatra, Groupwise registration of dynamic cardiac perfusion images using temporal information and segmentation information, in: In Proc: SPIE Medical Imaging, 2012 (2012).
- [78] D. Mahapatra, Neonatal brain mri skull stripping using graph cuts and shape priors, in: In Proc: MICCAI workshop on Image Analysis of Human Brain Development (IAHBD), 2011 (2011).
- [79] D. Mahapatra, Y. Sun, Orientation histograms as shape priors for left ventricle segmentation using graph cuts, in: In Proc: MICCAI, 2011, pp. 420–427 (2011).
- [80] D. Mahapatra, Y. Sun, Joint registration and segmentation of dynamic cardiac perfusion images using mrfs., in: Proc. MICCAI, 2010, pp. 493–501 (2010).
- [81] D. Mahapatra, Y. Sun., An mrf framework for joint registration and segmentation of natural and perfusion images, in: Proc. IEEE ICIP, 2010, pp. 1709–1712 (2010).
- [82] D. Mahapatra, Y. Sun, Retrieval of perfusion images using cosegmentation and shape context information, in: Proc. APSIPA Annual Summit and Conference (ASC), 2010 (2010).
- [83] D. Mahapatra, Y. Sun, A saliency based mrf method for the joint registration and segmentation of dynamic renal mr images, in: Proc. ICDIP, 2010 (2010).
- [84] D. Mahapatra, Y. Sun, Nonrigid registration of dynamic renal MR images using a saliency based MRF model, in: Proc. MICCAI, 2008, pp. 771–779 (2008).

- [85] D. Mahapatra, Y. Sun, Registration of dynamic renal MR images using neurobiological model of saliency, in: Proc. ISBI, 2008, pp. 1119–1122 (2008).
- [86] D. Mahapatra, M. Saini, Y. Sun, Illumination invariant tracking in office environments using neurobiology-saliency based particle filter, in: IEEE ICME, 2008, pp. 953–956 (2008).
- [87] D. Mahapatra, S. Roy, Y. Sun, Retrieval of mr kidney images by incorporating spatial information in histogram of low level features, in: In 13th International Conference on Biomedical Engineering, 2008 (2008).
- [88] D. Mahapatra, Y. Sun, Using saliency features for graphcut segmentation of perfusion kidney images, in: In 13th International Conference on Biomedical Engineering, 2008 (2008).
- [89] D. Mahapatra, S. Winkler, S. Yen, Motion saliency outweighs other low-level features while watching videos, in: SPIE HVEL., 2008, pp. 1–10 (2008).
- [90] D. Mahapatra, A. Routray, C. Mishra, An active snake model for classification of extreme emotions, in: IEEE International Conference on Industrial Technology (ICIT), 2006, pp. 2195–2199 (2006).
- [91] D. Mahapatra, B. Antony, S. Sedai, R. Garnavi, Deformable medical image registration using generative adversarial networks, in: In Proc. IEEE ISBI, 2018, pp. 1449–1453 (2018).
- [92] M. Saini, B. Guthier, H. Kuang, D. Mahapatra, A. Saddik, szoom: A framework for automatic zoom into high resolution surveillance videos, in: arXiv preprint arXiv:1909.10164, 2019 (2019).
- [93] B. Bozorgtabar, D. Mahapatra, H. von Teng, A. Pollinger, L. Ebner, J.-P. Thiran, M. Reyes, Informative sample generation using class aware generative adversarial networks for classification of chest xrays, in: arXiv preprint arXiv:1904.10781, 2019 (2019).

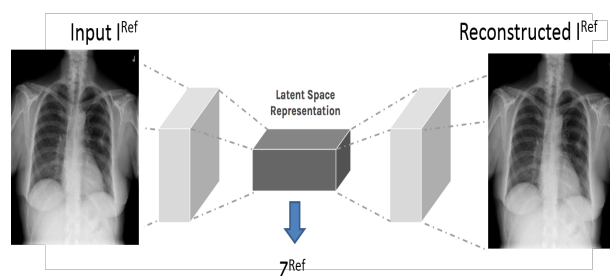
- [94] D. Mahapatra, Amd severity prediction and explainability using image registration and deep embedded clustering, in: arXiv preprint arXiv:1907.03075, 2019 (2019).
- [95] D. Mahapatra, Z. Ge, Combining transfer learning and segmentation information with gans for training data independent image registration, in: arXiv preprint arXiv:1903.10139, 2019 (2019).
- [96] D. Mahapatra, B. Bozorgtabar, Progressive generative adversarial networks for medical image super resolution, in: arXiv preprint arXiv:1902.02144, 2019 (2019).
- [97] S. Kuanar, K. Rao, D. Mahapatra, M. Bilas, Night time haze and glow removal using deep dilated convolutional network, in: arXiv preprint arXiv:1902.00855, 2019 (2019).
- [98] Z. Ge, D. Mahapatra, S. Sedai, R. Garnavi, R. Chakravorty, Chest x-rays classification: A multi-label and fine-grained problem, in: arXiv preprint arXiv:1807.07247, 2018 (2018).
- [99] D. Mahapatra, S. Sedai, R. Garnavi, Elastic registration of medical images with gans, in: arXiv preprint arXiv:1805.02369, 2018 (2018).
- [100] D. Mahapatra, B. Bozorgtabar, Retinal vasculature segmentation using local saliency maps and generative adversarial networks for image super resolution, in: arXiv preprint arXiv:1710.04783, 2017 (2017).
- [101] D. Mahapatra, Consensus based medical image segmentation using semi-supervised learning and graph cuts, in: arXiv preprint arXiv:1612.02166, 2017 (2017).
- [102] D. Mahapatra, K. Agarwal, R. Khosrowabadi, D. Prasad, Recent advances in statistical data and signal analysis: Application to real world diagnostics from medical and biological signals, in: Computational and mathematical methods in medicine, 2016 (2016).

- [103] P. Bastide, I. Kiral-Kornek, D. Mahapatra, S. Saha, A. Vishwanath, S. V. Cavallar, Crowdsourcing health improvements routes, in: US Patent App. 15/611,519, 2019 (2019).
- [104] D. Mahapatra, R. Garnavi, P. Roy, R. Tennakoon, System and method to teach and evaluate image grading performance using prior learned expert knowledge base, in: US Patent App. 15/459,457, 2018 (2018).
- [105] D. Mahapatra, R. Garnavi, P. Roy, R. Tennakoon, System and method to teach and evaluate image grading performance using prior learned expert knowledge base, in: US Patent App. 15/814,590, 2018 (2018).
- [106] D. Mahapatra, R. Garnavi, S. Sedai, R. Tennakoon, Generating an enriched knowledge base from annotated images, in: US Patent App. 15/429,735, 2018 (2018).
- [107] C. Peng, N. Wang, J. Li, X. Gao, Diface: Deep local descriptor for cross-modality face recognition., Pattern Recognition 90 (2019) 161171 (2019).
- [108] P. Bastide, I. Kiral-Kornek, D. Mahapatra, S. Saha, A. Vishwanath, S. V. Cavallar, Visual health maintenance and improvement, in: US Patent 9,993,385, 2018 (2018).
- [109] D. Mahapatra, R. Garnavi, S. Sedai, R. Tennakoon, Classification of severity of pathological condition using hybrid image representation, in: US Patent App. 15/426,634, 2018 (2018).
- [110] P. Bastide, I. Kiral-Kornek, D. Mahapatra, S. Saha, A. Vishwanath, S. V. Cavallar, Machine learned optimizing of health activity for participants during meeting times, in: US Patent App. 15/426,634, 2018 (2018).
- [111] D. Mahapatra, R. Garnavi, S. Sedai, R. Tennakoon, R. Chakravorty, Early prediction of age related macular degeneration by image reconstruction, in: US Patent App. 15/854,984, 2018 (2018).

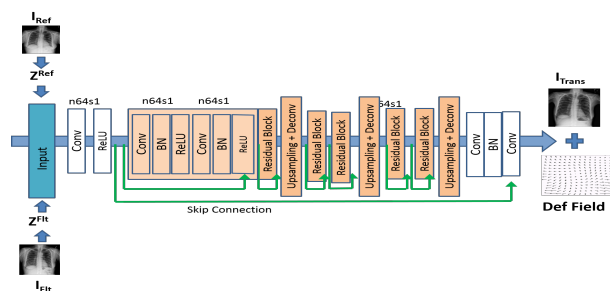
- [112] D. Mahapatra, R. Garnavi, S. Sedai, R. Tennakoon, R. Chakravorty, Early prediction of age related macular degeneration by image reconstruction, in: US Patent 9,943,225, 2018 (2018).
- [113] R. Shang, Y. Meng, W. Wang, F. Shang, L. Jiao, Local discriminative based sparse subspace learning for feature selection., *Pattern Recognition* 92 (2019) 219–230 (2019).
- [114] D. Mahapatra, R. Garnavi, S. Sedai, P. Roy, Retinal image quality assessment, error identification and automatic quality correction, in: US Patent 9,779,492, 2017 (2017).
- [115] D. Mahapatra, R. Garnavi, S. Sedai, P. Roy, Joint segmentation and characteristics estimation in medical images, in: US Patent App. 15/234,426, 2017 (2017).
- [116] X. Yang, W. Wu, Y. Chen, X. Li, J. Zhang, D. Long, L. Yang, An integrated inverse space sparse representation framework for tumor classification., *Pattern Recognition* 93 (2019) 293–311 (2019).
- [117] B. Lei, K. Jinman, E. Ahn, A. Kumar, F. Dagan, M. Fulham, Step-wise integration of deep class-specific learning for dermoscopic image segmentation., *Pattern Recognition* 85 (2019) 78–89 (2019).
- [118] H. Yang, C. Yuan, B. Li, Y. Du, J. Xing, W. Hu, S. Maybank, Asymmetric 3d convolutional neural networks for action recognition., *Pattern Recognition* 85 (2019) 1–12 (2019).
- [119] W. Wang, H. Wang, Z. Zhang, C. Zhang, Y. Gao, Semi-supervised domain adaptation via fredholm integral based kernel methods., *Pattern Recognition* 85 (2019) 185–197 (2019).
- [120] L. Hou, V. Nguyen, A.B.Kanevsky, D. Samaras, T. M. Kurc, T. Zhao, R. Gupta, Y. Gao, W. Chen, D. Foran, J. Saltz, Sparse autoencoder for unsupervised nucleus detection and representation in histopathology images., *Pattern Recognition* 86 (2019) 188–200 (2019).

- [121] I. Goodfellow, J. Pouget-Abadie, M. Mirza, B. Xu, D. Warde-Farley, S. Ozair, A. Courville, Y. Bengio, Generative adversarial nets, in: Proc. NIPS, 2014, pp. 2672–2680 (2014).
- [122] C. Ledig, L. Theis, F. Huszr, J. Caballero, A. Cunningham, A. Acosta, A. Aitken, A. Tejani, J. Totz, Z. Wang, W. Shi, Photo-realistic single image super-resolution using a generative adversarial network, in: CVPR, 2017, pp. 4681–4690 (2017).
- [123] D. Mahapatra, B. Bozorgtabar, S. Hewavitharanage, R. Garnavi, Image super resolution using generative adversarial networks and local saliency maps for retinal image analysis, in: MICCAI, 2017, pp. 382–390 (2017).
- [124] P. Isola, J. Zhu, T. Zhou, A. Efros, Image-to-image translation with conditional adversarial networks, in: IEEE CVPR, 2017 (2017).
- [125] J. Zhu, T. Park, P. Isola, A. Efros, Unpaired image-to-image translation using cycle-consistent adversarial networks, in: IEEE ICCV, 2017, pp. 2223–2232 (2017).
- [126] D. Rueckert, L. Sonoda, C. Hayes, D. Hill, M. Leach, D. Hawkes., Non-rigid registration using free-form deformations: application to breast mr images., *IEEE Trans. Med. Imag.*. 18 (8) (1999) 712–721 (1999).
- [127] Z. Wang, et. al., Image quality assessment: from error visibility to structural similarity., *IEEE Trans. Imag. Proc.* 13 (4) (2004) 600–612 (2004).
- [128] K. Simonyan, A. Zisserman., Very deep convolutional networks for large-scale image recognition, *CoRR abs/1409.1556* (2014).
- [129] X. Wang, Y. Peng, L. Lu, Z. Lu, M. Bagheri, R. Summers, Chestx-ray8: Hospital-scale chest x-ray database and benchmarks on weakly-supervised classification and localization of common thorax diseases, in: In Proc. CVPR, 2017 (2017).

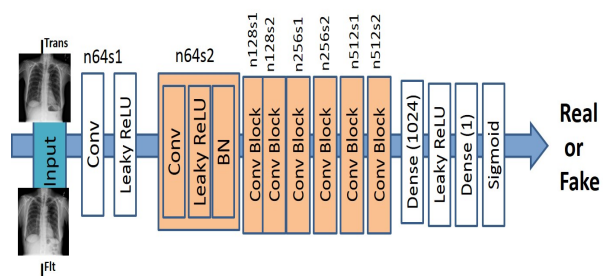
- [130] D. Kingma, J. Ba, Adam: A method for stochastic optimization, in: International Conference on Learning Representations,, 2014 (2014).
- [131] S. Klein, M. Staring, K. Murphy, M. Viergever, J. Pluim., Elastix: a toolbox for intensity based medical image registration., *IEEE Trans. Med. Imag.*. 29 (1) (2010) 196–205 (2010).
- [132] J. Deng, W. Dong, R. Socher, L.-J. Li, K. Li, L. Fei-Fei., ImageNet: A Large-Scale Hierarchical Image Database, in: *CVPR09, 2009* (2009).
- [133] S. G. Mueller, Ways toward an early diagnosis in alzheimers disease: the alzheimers disease neuroimaging initiative (ADNI)., *Alzheimers & Dementia* 1 (1) (2005) 55–66 (2005).
- [134] B. Fischl, Freesurfer, *Neuroimage* 62 (2) (2015) 774–781 (2015).
- [135] S. Hajeb, H. Rabbani, M. Akhlaghi., Diabetic retinopathy grading by digital curvelet transform., *Comput Math Methods Med.* (2012) 7619–01 (2012).
- [136] A. Frangi, W. Niessen, K. Vincken, M. Viergever, Multiscale vessel enhancement filtering, in: *MICCAI, 1998*, pp. 130–137 (1998).



(a)



(b)



(c)

Figure 1: (a) Convolutional Autoencoder architecture; (b) Generator Network; (c) Discriminator network. $n64s1$ denotes 64 feature maps (n) and stride (s) 1 for each convolutional layer.

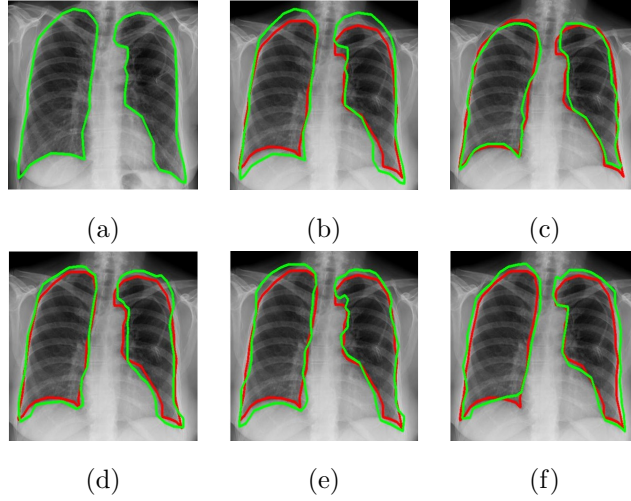


Figure 2: Results for **non-diseased** lung Xray image registration from NIH dataset (patient 5). (a) I_{Flt} with I_{Flt}^{Seg} (green); (b) I_{Ref} with I_{Ref}^{Seg} (red) and I_{Flt}^{Seg} before registration; Superimposed registered mask obtained using: (c) $UReg - Net$; (d) $DIR - Net$; (e) $JRS - Net$; (f) $Elastix$.

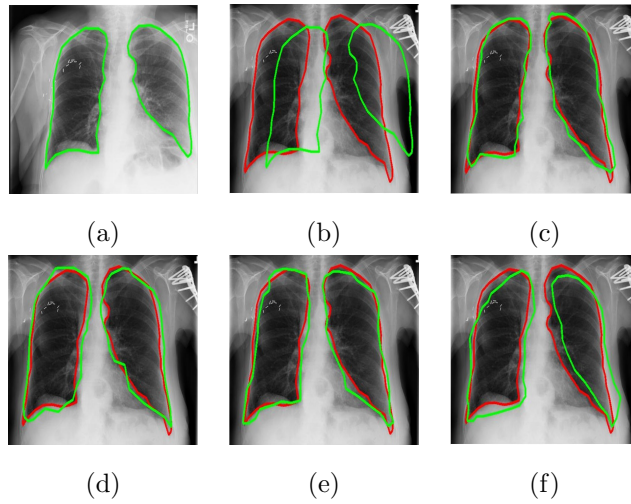


Figure 3: Results for **diseased** lung Xray images from NIH dataset (patient 5). (a) I_{Flt} with I_{Flt}^{Seg} (green); (b) I_{Ref} with I_{Ref}^{Seg} (red) and I_{Flt}^{Seg} before registration; Superimposed registered mask obtained using: (c) $UReg - Net$; (d) $DIR - Net$; (e) $JRS - Net$; (f) $Elastix$.

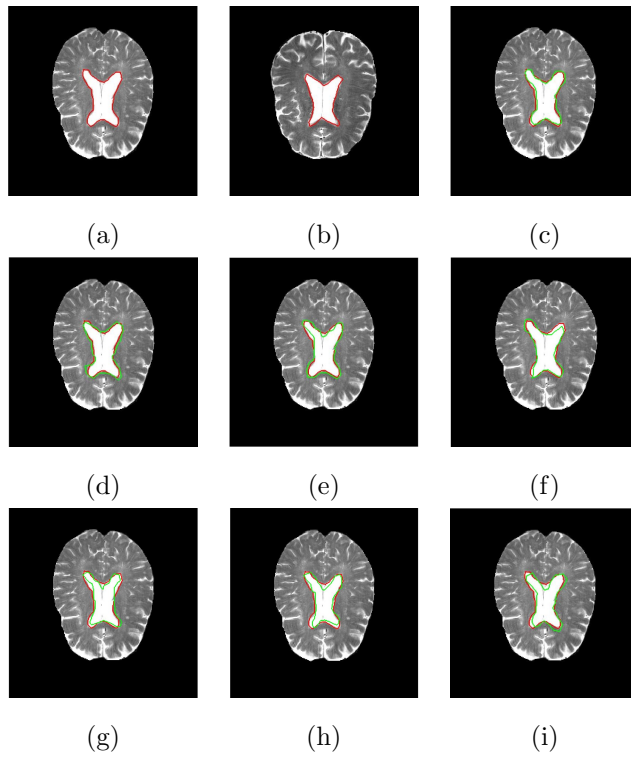


Figure 4: Results for atlas based brain MRI image registration. (a) I_{Ref} with I_{Ref}^{Seg} (b) I_{Flt} with I_{Flt}^{Seg} . Superimposed registered mask (in green) obtained using: (c) $UReg - Net$; (d)[6]; (e) $URegImage$; (f) $DIR - Net$; (g) $JRS - Net$; (f) [43] and (g) $Elastix$.

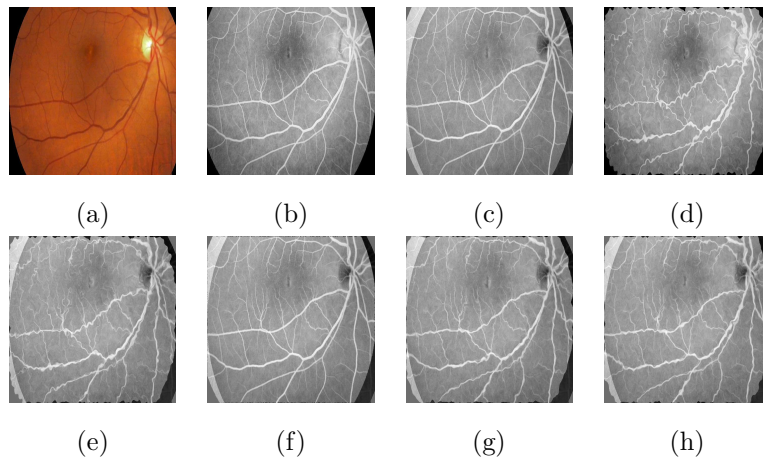


Figure 5: Example results for retinal fundus and FA registration. (a) Color fundus image; (b) Original FA image; (c) ground truth difference image before simulated deformation; (d) Deformed FA image or the floating image; Difference image (e) before registration; after registration using (f) *UReg-Net*; (g) *DIRNet*; (h) *Elastix* .